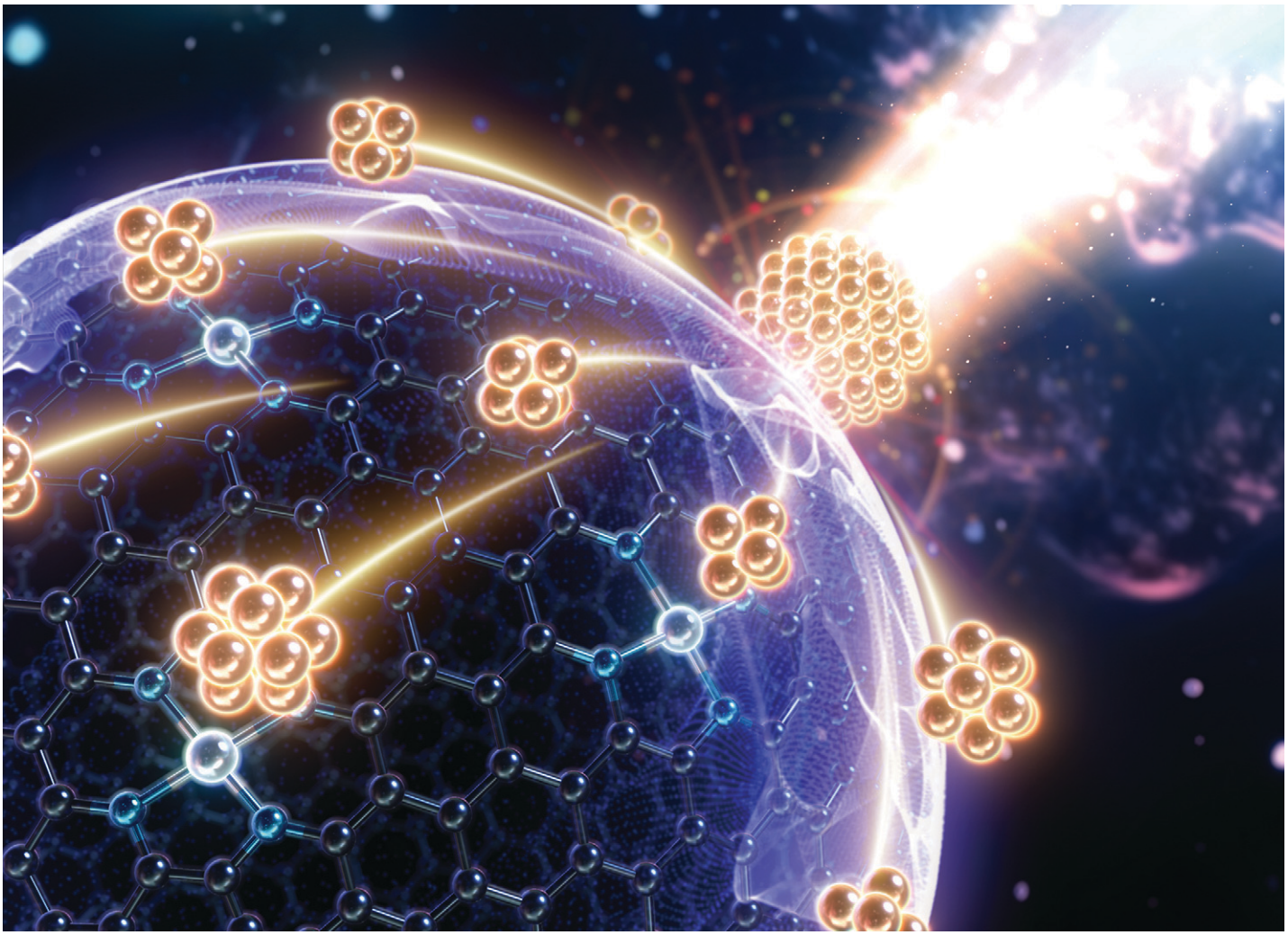

Showcasing research from New Field Pioneering Div., Toyota Boshoku Corp., Aichi, Japan.

Sustainable activation of the $PtCl_n$/Fe–N–C cathode for PEFCs through repeated subnanometer sizing and coarsening

We found that platinum ions that dissolve from platinum chloride are redeposited and interact with iron and nitrogen sites in the iron-nitrogen-carbon support as subnanometer platinum particles. This results in an increased electrochemical surface area and specific activity for the oxygen reduction reaction.

Image reproduced by permission of Hiroshi Yano from *RSC Appl. Interfaces*, 2025, **2**, 1621.

As featured in:

See Hiroshi Yano, *RSC Appl. Interfaces*, 2025, **2**, 1621.

ROYAL SOCIETY OF CHEMISTRY

rsc.li/RSCApplInter

Registered charity number: 207890

RSC Applied Interfaces

ROYAL SOCIETY OF CHEMISTRY

PAPER

View Article Online
View Journal | View Issue

Cite this: *RSC Appl. Interfaces*, 2025, **2**, 1621

Sustainable activation of the $PtCl_n$/Fe–N–C cathode for PEFCs through repeated subnanometer sizing and coarsening

Hiroshi Yano

In recent years, the development of polymer electrolyte fuel cells has been in transition from application in fuel cell vehicles and residential cogeneration systems to heavy-duty vehicles such as trucks and buses. Therefore, higher durability and performance are required for each component material, and the development of cathode catalysts is particularly important. We have recently developed a $PtCl_n$/Fe–N–C catalyst that is 8 times more active than standard Pt/C and maintains activity for 100 000 cycles under accelerated stress testing. This is because Pt ions dissolved from $PtCl_n$ are redeposited and interact with Fe and N sites in the support as subnanometer Pt particles ($Pt_{subnano}$), which results in an increased electrochemical surface area and specific activity for the oxygen reduction reaction. In the present research, Cl in $PtCl_n$ was determined to play an important role in promoting the formation of $Pt_{subnano}$, and the details of the $Pt_{subnano}$ formation process, which is the repetitive aggregation and subnano-sizing of Pt in a very short period of the potential cycle, were elucidated by *in situ* X-ray absorption fine structure analysis.

Received 30th June 2025,
Accepted 24th August 2025

DOI: 10.1039/d5lf00185d

rsc.li/RSCApplInter

Introduction

Polymer electrolyte fuel cells (PEFCs) are currently used as the primary power source for zero-emission fuel cell vehicles (FCVs) and residential cogeneration systems such as Ene·Farm, and the market for PEFCs is growing every year. There has been a strong desire to develop fuel cells in recent years for heavy-duty vehicles (HDVs) that are difficult to electrify with batteries alone, such as trucks, buses, rail vehicles, ships, construction equipment, and industrial vehicles, because environmental regulations have tightened and decarbonization policies have been promoted in many countries. Fuel cells in HDV applications must have higher performance than that of current FCVs, including higher power density and longer operating time. According to the "Fuel Cell Roadmap for HDVs (2024 version)" published by the New Energy and Industrial Technology Development Organization (NEDO) in Japan,[1] the 2030 targets for power density, durability, and Pt usage are 0.60 kW L^{-1}, 50 000 h, and 0.19 g(Pt) kW^{-1}, respectively. To achieve these goals, it is essential to improve the performance of all constituent materials, although breakthroughs in catalyst development are particularly important.

Many Pt catalysts are used in PEFC cathodes, and the oxygen reduction reaction (ORR) activity per unit mass of Pt (mass activity; MA) is commonly used as a measure of catalytic performance. The MA is related to the specific activity (SA) and the electrochemical surface area (ECSA) as follows:

$$\mathrm{MA}\ (\mathrm{A\ g_{Pt}^{-1}}) = \mathrm{SA}\ (\mathrm{A\ m^{-2}}) \times \mathrm{ECSA}\ (\mathrm{m^2\ g_{Pt}^{-1}}). \quad (1)$$

The best way to significantly increase the MA is thus to increase both the SA and ECSA simultaneously. The increase in SA by alloying with non-noble metals such as Fe, Co, and Ni has been investigated over the past few decades, and various developments have been made, including ordered alloys,[2–4] disordered alloys,[5,6] nanoframe types,[7,8] and core-shell types.[9,10] In all cases, the SA values were improved by a factor of 2 to 8 compared to Pt. The problem is that de-alloying cannot be suppressed during PEFC operation, so that high SA values cannot be maintained.

To increase the ECSA, the Pt particle size (d) should be as small as possible because the ECSA value increases in inverse proportion to d. However, if the size is reduced too close to the atomic level (aggregates of a few to several tens of atoms, called cluster catalysts), the expected ECSA values based on the spherical approximation will not be obtained. For example, the specific surface area (SSA) of a Pt_6 cluster catalyst consisting of six Pt atoms is estimated to be approximately 500 $m^2\ g^{-1}$; however, the actual ECSA value is 40–70 $m^2\ g^{-1}$,[11–13] which corresponds to an SSA equivalent to d = 7–4 nm. It is considered that the change in the hydrogen

New Field Pioneering Division, Toyota Boshoku Corp, Kariya, Aichi 448-8651, Japan. E-mail: hiroshi.yano@toyota-boshoku.com

adsorption energy for Pt contributes to this phenomenon.[14,15] The dependence of the SSA and the ECSA on the particle size has been verified experimentally.[16] The minimum size at which 100% of the electrochemically active area (ECAA, = ECSA/SSA × 100%) of the Pt particles can be maintained is 1.3 to 1.4 nm. As the particle size decreases below 1.3 nm, the increase in ECSA deviates from the 1/d trajectory with ECSA < SSA. Therefore, there is a limit to the increase in the ECSA due to the size effect.

The unique properties of certain carbon materials have been explored to improve the performance of Pt nanoparticles. Mesoporous carbon[17–19] is a prime example, with a high SSA, controllable pore structure, excellent electrical conductivity, and chemical stability, all of which are important factors for improving catalyst efficiency and durability. However, improvement of the carbon properties alone is not sufficient to achieve the PEFC targets for HDVs. N-doped carbon with a small amount of Fe (Fe–N–C) has recently been shown to be an excellent alternative to the most advanced carbon support materials. When Pt is supported on Fe–N–C catalysts, the durability is improved because the Pt is firmly immobilized by the Fe and the aggregation of Pt is suppressed.[20–22]

We recently reported on the development and performance of a highly functionalized catalyst consisting of Pt chloride ($PtCl_n$) and Fe–N–C ($PtCl_n$/Fe–N–C).[23] The ECSA of the $PtCl_n$/Fe–N–C catalyst did not decrease at all after 100 000 cycles of exposure to accelerated stress testing (AST) due to the *in situ* formation of subnano-sized Pt particles ($Pt_{subnano}$) on the Fe and N sites of Fe–N–C. The SA was also improved due to the alloying effect of Pt and Fe bonding. We consider that the functional elucidation and application of this catalyst, which combines subnano-sizing of Pt particles with durability, is very important for the development of practical catalysts for HDVs. In the present research, the fundamental electrochemical properties of $PtCl_n$/Fe–N–C were investigated to determine the role of chlorine, and the process of $Pt_{subnano}$ formation was further investigated using *in situ* X-ray absorption fine structure (XAFS) techniques.

Experimental

Preparation of catalysts

The $PtCl_n$/Fe–N–C catalysts were prepared in a manner similar to that described previously.[23] 60 mg of hexachloroplatinic acid hydrogen(IV) hexahydrate ($H_2PtCl_6{\cdot}6H_2O$, Kanto Chemical, Japan) and 50 mg of Fe–N–C doped carbon (the Fe and N concentrations in the carbon were 0.5 and 5 wt%, respectively), prepared by the hard template method using fumed silica,[24,25] were mixed in ethanol (1 mL) in a mortar. The $PtCl_n$ particle size was well-controlled by varying the $H_2PtCl_6{\cdot}6H_2O$ concentration.[16] The mixture was stirred while the materials were warmed using a heat gun until most of the ethanol evaporated. The resultant powder was completely dried by heating at 60 °C for 30 min under vacuum. Unless otherwise noted, the powder was then heat treated in a tube furnace at 200 °C for 2 h in an Ar atmosphere. The metal weight percent in each powder was estimated from the weight loss by thermogravimetry (TG) analysis.

Accelerated stress testing (AST)

The working electrode was prepared by the uniform dispersion of $PtCl_n$/Fe–N–C on a glassy carbon disk substrate (∅ 4 mm) followed by Nafion coating, similar to our previous work.[23] The AST was performed using a rotating disk electrode (RDE) system (RRDE-3A, ALS Co., Ltd) with a gastight water-jacketed Pyrex glass cell. Details of the AST procedure for the catalysts have been described elsewhere.[23] In the first step, cyclic voltammetry (CV) data were recorded in a 0.1 M $HClO_4$ solution deaerated with Ar at 30 °C at the scan rate of 0.05 V s^{-1} between 0.05 V and 1.0 V. Initial holding potential and time were 0.05 V and 2 s, respectively. The ECSA value was calculated from eqn (2).

$$\mathrm{ECSA} = Q_H/(\Delta Q_H \times m_{Pt}), \quad (2)$$

where Q_H is hydrogen adsorption waves observed around 0.05 V to 0.4 V (see Fig. S1 of the SI) was calculated by integration, ΔQ_H (210 μC cm^{-2}) is electric charge for the hydrogen adsorption for bulk polycrystalline Pt,[26,27] m_{Pt} is the amount of Pt deposited on the working electrode. In the second step, hydrodynamic voltammetry data for the ORR were recorded from 0.3 to 1.0 V at 10 mV s^{-1} in O_2-saturated 0.1 M $HClO_4$ solution at 30 °C. An example of a Nafion-coated $PtCl_n$/Fe–N–C electrode is shown in Fig. S2(A) of the SI. The kinetically controlled current I_k, at constant potential was calculated using the Koutecky–Levich equation:

$$1/I = 1/I_k + 1/(0.62nFSD^{2/3}C_O v^{-1/6}\omega^{1/2}), \quad (3)$$

where n is the number of electrons transferred, F is the Faraday constant, S is the effective projected area of the Pt catalyst, D is the diffusion coefficient of O_2, C_O is the O_2 concentration, v is the viscosity of the electrolyte, and ω is the angular velocity. I^{-1} *versus* $\omega^{1/2}$ plots for the ORR at 0.85 V are shown in Fig. S2(B). A linear relationship with a constant slope was obtained. Values of I_k could be calculated by extrapolation of the plots to $\omega^{1/2} = 0$. SA_k and MA_k were determined by dividing I_k by the S and the amount of Pt initially loaded on the disk electrode, respectively. In the third step, the electrode was subjected to accelerated degradation by potential step cycling through square waves from 0.6 V to 1.0 V (each potential held for 3 s) in 0.1 M $HClO_4$ solution deaerated with Ar.[23,28] After a specific number of potential step cycles (N), the step 1 procedure was repeated.

XRD, XPS, and TEM analysis

The catalyst powders were analyzed using X-ray diffraction (XRD, Rigaku Ultima IV) with Cu Kα radiation (40 kV, 40 mA)

to obtain the information on the crystal structure. The XRD patterns were collected with 2θ values between 15° and 90° at a scan rate of 1 deg min^{-1}. X-ray photoelectron spectroscopy (XPS) was used to measure the electronic state of the Pt and Cl in the catalyst powders. The XPS data were collected using a spectrometer (PHI ESCA-5800) with a monochromatic Al Kα source operated at 300 W with a photoelectron takeoff angle of 45°, which corresponds to a measurement depth of 4 nm. Transmission electron microscopy (TEM, Hitachi H-9500, acceleration voltage = 200 kV; JEOL, JEM-F200, acceleration voltage = 200 kV) was used to obtain particle size distributions and electron diffraction (ED) patterns. All distributions presented were obtained for 300 particles from several TEM micrographs.

In situ XAFS measurements

XAFS spectra in the L-edge region for Pt was measured at the BL5S1 beamline of AichiSR equipped with a Si(111) monochromator and multichannel silicon drift detector. All spectra were recorded in fluorescence mode. Images of the electrochemical cell and working electrode are shown in Fig. S3 of the SI. The cell, which was provided by Nissan ARC, is made of Teflon and the X-ray window is made of a polyimide film. The catalyst suspension was prepared by mixing 2 mg of catalyst powder with 2 mL of ethanol, followed by ultrasonication for 10 s. Catalyst ink (24 μL) matched to the AST test in the previous section in terms of the amount of the Pt loading (~6 μg) was then dropped onto a 3 mm (width) × 2 mm (length) × 0.5 mm (depth) sized ditch created on a glassy carbon plate. Nafion solution was then dropped onto the catalyst layer and dried in air at 60 °C. AST was performed in 0.1 M $HClO_4$ solution at room temperature. Although the TEM images and ED patterns shown in Fig. 7 and the XPS spectra in Fig. 8 were obtained from different experiments from the *in situ* XAFS measurements, all conditions, including catalyst, electrode preparation conditions, and cell, were the same as those for the *in situ* XAFS measurements.

Results and discussion

Role of Cl_n in $PtCl_n$

The effect of Cl_n on the catalytic performance of $PtCl_n$/Fe–N–C was first investigated. One of the catalysts examined was a conventional $PtCl_n$/Fe–N–C (heat treated for 2 h at 200 °C under an Ar atmosphere), which was prepared following the method described in the Experimental section. The other catalyst was prepared by a multi-step heat treatment at 200 °C for 2 h, 400 °C for 4 h, and 500 °C for 2 h under a 3% H_2 atmosphere (described as $PtCl_n$/Fe–N–C–HT(H_2)) to reduce Pt and remove Cl_n while minimizing particle aggregation.

Fig. 1 shows XRD patterns for $PtCl_n$/Fe–N–C, $PtCl_n$/Fe–N–C–HT(H_2), and standard commercial Pt/C (TEC10E50E, TKK) powders. The broad peak at 2θ = ~25° for all samples was assigned to the (002) planes of graphite carbon in the carbon material support. No peaks attributable to Pt were detected

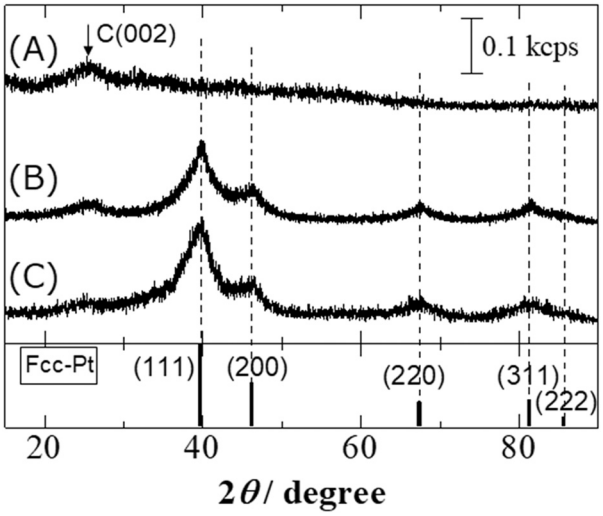

Fig. 1 XRD patterns for pristine powders of (A) $PtCl_n$/Fe–N–C, (B) $PtCl_n$/Fe–N–C–HT(H_2), and (C) commercial Pt/C.

in the XRD pattern for $PtCl_n$/Fe–N–C, because the $PtCl_n$ particles are very small and exist as Pt chloride with low crystallinity, as previously reported.[23] In contrast, the XRD pattern for $PtCl_n$/Fe–N–C–HT(H_2) was very similar to that for the commercial standard catalyst (Pt/C). The diffraction peaks were assigned to the (111), (200), (220), (311), and (222) planes of face-centered cubic (fcc) Pt. The average crystallite size (d_{XRD}) was 2.2 nm, which was calculated using the Scherrer equation for the XRD 220 peak (~67°). No additional peaks assigned to Fe, or Fe compounds such as oxides were identified. In addition, the complete disappearance of chlorine is evident in the XPS spectrum in Fig. S4 of the SI. $PtCl_n$/Fe–N–C–HT(H_2) was thus found to be

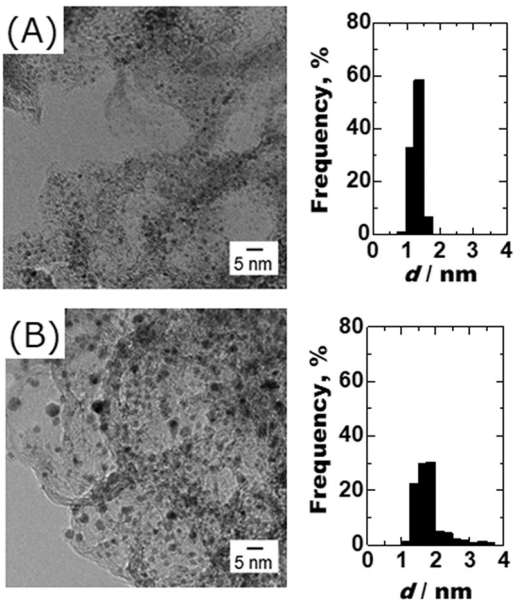

Fig. 2 TEM images and particles size distributions for (A) $PtCl_n$/Fe–N–C and (B) Pt/Fe–N–C powders.

loaded with pure Pt particles. In the following discussion, the $PtCl_n$/Fe–N–C–HT(H_2) catalyst is referred to as Pt/Fe–N–C.

Fig. 2 shows TEM images and particle size distributions for the $PtCl_n$/Fe–N–C and Pt/Fe–N–C powders. The average particle size (d_{TEM}) and standard deviation for $PtCl_n$/Fe–N–C was 1.3 ± 0.1 nm. In contrast, d_{TEM} for Pt/Fe–N–C was 1.7 ± 0.4 nm, which is significantly larger. The distribution was also extended to the larger particle size side; the frequency of particles larger than 2 nm accounted for more than 15% of the total. It could be presumed that the presence of these larger particles is the reason why the d_{XRD} value (2.2 nm) is larger than the d_{TEM} value (1.7 nm).

Fig. 3 and 4 show cyclic voltammograms (CVs) and the ECSA values for Nafion-coated $PtCl_n$/Fe–N–C and Pt/Fe–N–C electrodes, respectively. The hydrogen adsorption/desorption curve (between 0.05 V and 0.45 V) was not significantly changed at the $PtCl_n$/Fe–N–C electrode and the ECSA value remained almost constant. However, the ECSA began to increase after N = 70 000. This phenomenon is due to the repeated dissolution and redeposition of Pt particles during the potential cycle, which results in the *in situ* formation of ultrafine subnanoscale Pt particles ($Pt_{subnano}$). These particles work well as catalysts, as reported previously.[23] The single-cell with 25 cm^2 membrane electrode assembly (MEA) test at 80 °C also revealed that ECSA remained constant at the

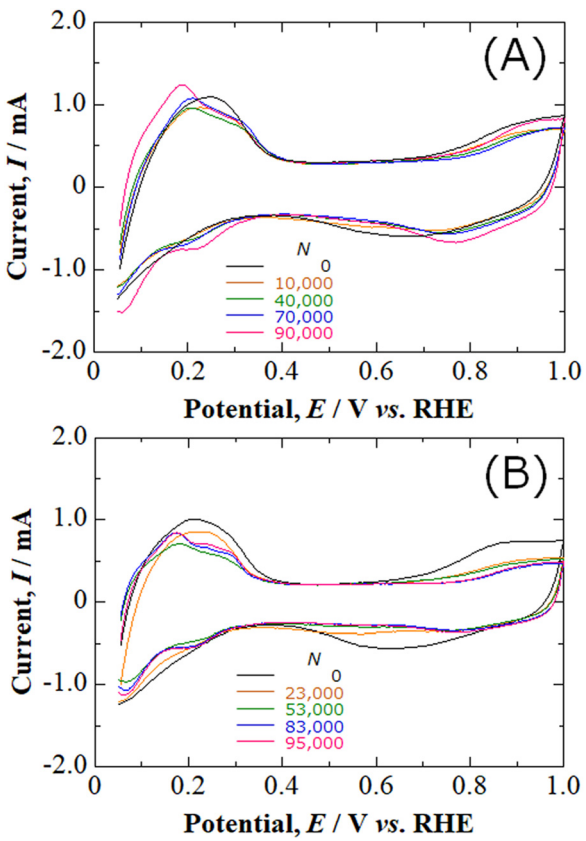

Fig. 3 Cyclic voltammograms to determine the ECSA for Nafion-coated (A) $PtCl_n$/Fe–N–C and (B) Pt/Fe–N–C electrodes in 0.1 M $HClO_4$ solution deaerated with Ar at 25 °C.

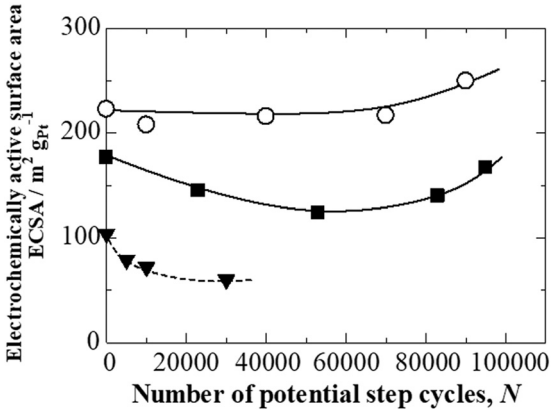

Fig. 4 ECSA for Nafion-coated (○) $PtCl_n$/Fe–N–C, (■) Pt/Fe–N–C, and (▼) commercial Pt/C electrodes as a function of N.

$PtCl_n$/Fe–N–C cathode (as shown in Fig. S5 in the SI). Therefore, it is inferred that this catalyst forms $Pt_{subnano}$ even in the operational atmosphere of PEFCs. In contrast, the ECSA value for the Pt/Fe–N–C electrode decreased as N increased to N = 60 000 and the hydrogen adsorption/desorption curve was significantly smaller. This is the same trend and general phenomenon observed for standard Pt/C catalysts, and suggests that particle aggregation is more likely than Pt dissolution and redeposition in highly crystallized Pt particles. However, above N = 60 000, the ECSA increased for $PtCl_n$/Fe–N–C. The dissolution and reprecipitation of Pt may thus predominate, which results in the aggressive formation of ultrafine particles. The standard Pt/C catalyst was only recorded up to N = 30 000, although ECSA is expected to decrease with increasing N. The dependence of the ECSA on the carbon support species (*e.g.*, mesoporous carbon and graphitized carbon black) has been studied in previous work,[23] and the increase in ECSA (*i.e.*, the formation of ultrafine particles) is a phenomenon unique to catalysts using Fe–N–C as a support. These results suggest that the dissolution rate of Pt on Fe–N–C is one of the most important factors to maintain the ECSA. Therefore, an attempt was made to adjust the particle size of $PtCl_n$ to be smaller than d = 1.3 nm, so that Pt could be easily dissolved during the catalytic reaction. In the following discussion, $PtCl_n$/Fe–N–C catalysts with various d are denoted as $(PtCl_n)_{d\text{nm}}$/Fe–N–C.

Effect of particle size (d)

Two types of $(PtCl_n)_{d\text{nm}}$/Fe–N–C catalysts were prepared with different d values. In addition, two of each catalyst type were prepared to verify reproducibility. Catalysts prepared for confirmation of reproducibility are marked with an asterisk (*e.g.*, *[$(PtCl_n)_{d\text{nm}}$/Fe–N–C]). The conditions for the preparation of these catalysts are summarized in Table 1. The concentrations of $H_2PtCl_6{\cdot}6H_2O$ during synthesis were adjusted to 0.12 and 0.05 mol L^{-1} to achieve d = 1.3 and 0.9 nm, respectively. Fig. 5 shows TEM images and particle size distributions for the $(PtCl_n)_{1.3\text{nm}}$/Fe–N–C, *[$(PtCl_n)_{1.3\text{nm}}$/Fe–N–

Table 1 Conditions for the preparation of $(PtCl_n)_{dnm}$/Fe–N–C

Catalysts	$H_2PtCl_6{\cdot}6H_2O$[a] (mol L^{-1})	Metal loaded[b] (wt%)	d[c] (nm)
$(PtCl_n)_{1.3nm}$/Fe–N–C	0.12	26.7	1.3 ± 0.1
*[$(PtCl_n)_{1.3nm}$/Fe–N–C]	0.12	24.1	1.4 ± 0.2
$(PtCl_n)_{0.9nm}$/Fe–N–C	0.05	18.9	0.9 ± 0.1
*[$(PtCl_n)_{0.9nm}$/Fe–N–C]	0.05	17.0	1.0 ± 0.1

[a] Concentration of $H_2PtCl_6{\cdot}6H_2O$ in 1 mL EtOH. [b] The metal weight percent estimated by weight loss using TG. [c] The average particle size and standard deviation were obtained among 300 particles.

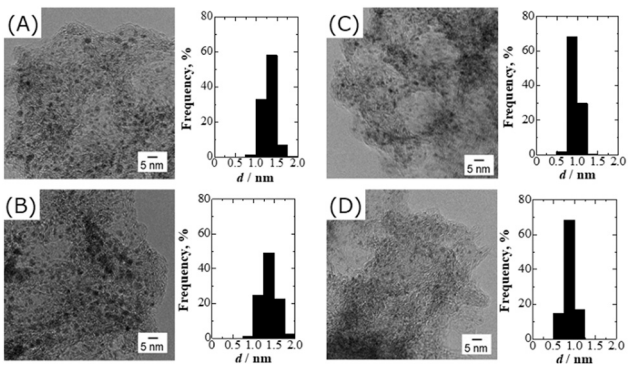

Fig. 5 TEM images and particle size distributions for (A) $(PtCl_n)_{1.3nm}$/Fe–N–C, (B) *[$(PtCl_n)_{1.3nm}$/Fe–N–C], (C) $(PtCl_n)_{0.9nm}$/Fe–N–C, and (D) *[$(PtCl_n)_{0.9nm}$/Fe–N–C] powders.

C], $(PtCl_n)_{0.9nm}$/Fe–N–C, and *[$(PtCl_n)_{0.9nm}$/Fe–N–C] catalysts powders. The prepared $(PtCl_n)_{dnm}$ were uniformly dispersed on the Fe–N–C support and their size distributions were fairly narrow compared with the commercial Pt/C (as shown in Fig. S6 in the SI). The d values obtained from the particle size distributions for the $(PtCl_n)_{1.3nm}$/Fe–N–C and *[$(PtCl_n)_{1.3nm}$/Fe–N–C] catalysts were almost identical at 1.3 ± 0.1 nm and 1.4 ± 0.2 nm, respectively. The d values for the $(PtCl_n)_{0.9nm}$/Fe–N–C and *[$(PtCl_n)_{0.9nm}$/Fe–N–C] catalysts were also almost identical at 0.9 ± 0.1 nm and 1.0 ± 0.1 nm, respectively.

The effect of particle size on electrochemical properties was then examined using the same AST as presented in Fig. 3 and 4. Fig. 6 shows changes in the ECSA, kinetically controlled specific activity SA_k, and kinetically controlled mass activity MA_k, for the two types four electrodes as a function of N. The values at commercial Pt/C electrode were also plotted as reference. The initial ECSA values for the $(PtCl_n)_{1.3nm}$/Fe–N–C and *[$(PtCl_n)_{1.3nm}$/Fe–N–C] electrodes were 221 and 223 m^2 g^{-1}, respectively, which are very reasonable for the SSA calculated from d. The ECSA values for both these electrodes tended to remain constant up to approximately N = 60 000 and then increased slightly. SA_k decreased only slightly relative to the number of cycles. However, the SA_k value remains approximately 5 times higher than that of commercial Pt/C during the AST. Since the intrinsic activity of Fe–N–C is negligible,[2,3] it is believed that the maintenance of activity is mainly due to the PtFe alloy that is continuously formed during AST. Details will be described later. Both electrodes were consistent in their properties, and the change in the catalytic activity of the $(PtCl_n)_{1.3nm}$/Fe–N–C and *[$(PtCl_n)_{1.3nm}$/Fe–N–C] electrodes was highly reproducible. On the other hand, the ECSA values for the $(PtCl_n)_{0.9nm}$/Fe–N–C and *[$(PtCl_n)_{0.9nm}$/Fe–N–C] electrodes were 68.4 and 72.3 m^2 g^{-1}, respectively, which are considerably smaller than the SSA expected based on the measured d. The initial SA_k value was also less than half that for the $(PtCl_n)_{1.3nm}$/Fe–N–C electrode. We have previously

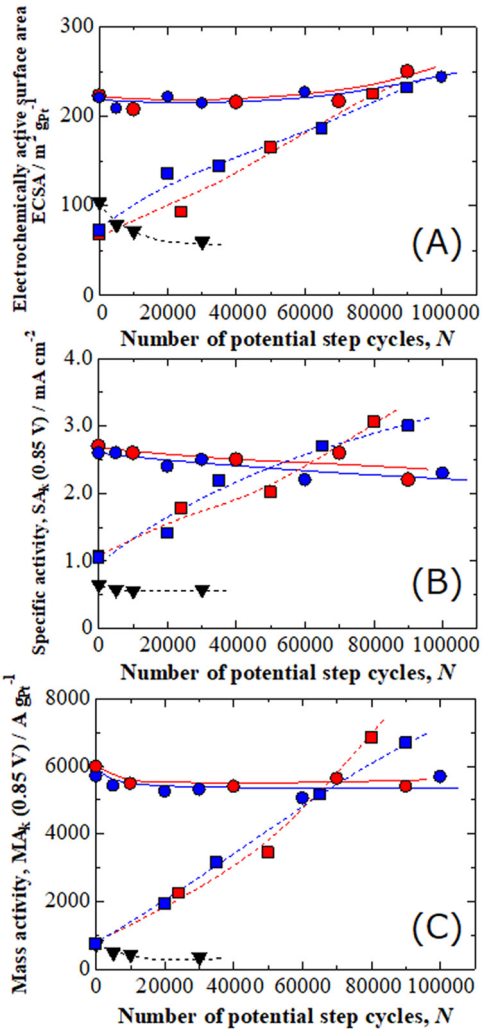

Fig. 6 (A) ECSA, (B) SA_k, and (C) MA_k for the ORR for Nafion-coated (●) $(PtCl_n)_{1.3nm}$/Fe–N–C, (●) *[$(PtCl_n)_{1.3nm}$/Fe–N–C], (■) $(PtCl_n)_{0.9nm}$/Fe–N–C, (■) *[$(PtCl_n)_{0.9nm}$/Fe–N–C], and (▼) commercial Pt/C electrodes as a function of N.

reported that the ECSA and the SA_k values of Pt particles are strongly affected by d.[16] When d is smaller than 1.3 nm, the hydrogen adsorption energy for Pt increases and the ECSA value tends to be smaller than the expected SSA value. At the same time, the adsorption energy for oxygen also changes and the SA_k value decreases.[16] However, the ECSA and SA_k values for the $(PtCl_n)_{0.9nm}$/Fe–N–C electrode increased with N to reach the value of the $(PtCl_n)_{1.3nm}$/Fe–N–C electrode at approximately N = 80 000. The same trend was also observed for the *$[(PtCl_n)_{0.9nm}$/Fe–N–C] electrode, which indicates that the reproducibility is very high.

The reason why the ECSA values are maintained for the $(PtCl_n)_{1.3nm}$/Fe–N–C electrode is that the dissolved Pt forms $Pt_{subnano}$ on Fe and N atoms in the Fe–N–C support during the potential cycle. The details have already been reported previously.[23] On the other hand, a very interesting trend that supports the $Pt_{subnano}$ formation mechanism was observed in the change in ECSA at the $(PtCl_n)_{0.9nm}$/Fe–N–C electrode. The ECSA increases with potential cycle number, which suggests that $Pt_{subnano}$ are more likely to form when Pt is dissolving at a faster rate. To elucidate the details of this phenomenon, the structural changes of Pt at the beginning of the potential cycle were investigated using ED, XPS, and *in situ* XAFS analysis.

In situ XAFS measurement

TEM, ED and XPS analyses were performed to investigate the morphological changes and electronic structure of the Pt particles. All measurements were obtained from separately prepared samples under the same conditions as those for the *in situ* XAFS measurements described below. Fig. 7 shows low- and high-magnification TEM images and ED patterns for $(PtCl_n)_{0.9nm}$/Fe–N–C before (N = 0, *i.e.* pristine powder) and after the AST (N = 25, 50, and 75 cycles, *i.e.* powder after electrochemical measurements). The formation of fine Pt particles ($Pt_{subnano}$) of *ca.* 0.5 nm (red arrow) after N = 25 cycles was confirmed by high-magnification TEM observation. The ED pattern at N = 0 showed only halo-like bands assigned to amorphous carbon. However, after 25 cycles, rings assigned to the (113), (022), (002), and (111) planes of fcc Pt were observed. This indicates that $PtCl_n$ was reduced to Pt during only 25 potential cycles. The XPS measurements also support these results. Fig. 8 shows XPS spectra in the Pt 4f and Cl 2p regions. The Pt 4f region has two doublet peaks (4f5/2 and 4f7/2 states), and in the case of N = 0, the peak position occurs at the binding energy of Pt(II) (72.4 and 75.6 eV). After N = 25, 50, and 75 cycles, the peak shifted to the same energy position on the low energy side (binding energy of Pt(0)). Simultaneously, the Cl 2p spectrum almost disappeared. The ED pattern also indicated that PtFe alloys begin to form after N = 50 cycles. Fig. 7(C) and (D) show ring patterns that could be assigned to PtFe alloy (*i.e.*, to (110) and (011) lattice planes) and PtFe (120) and Pt_3Fe (022) alloys were observed after N = 50 and 75 cycles, respectively. As shown in Fig. 6, the SA_k of $PtCl_n$/Fe–N–C

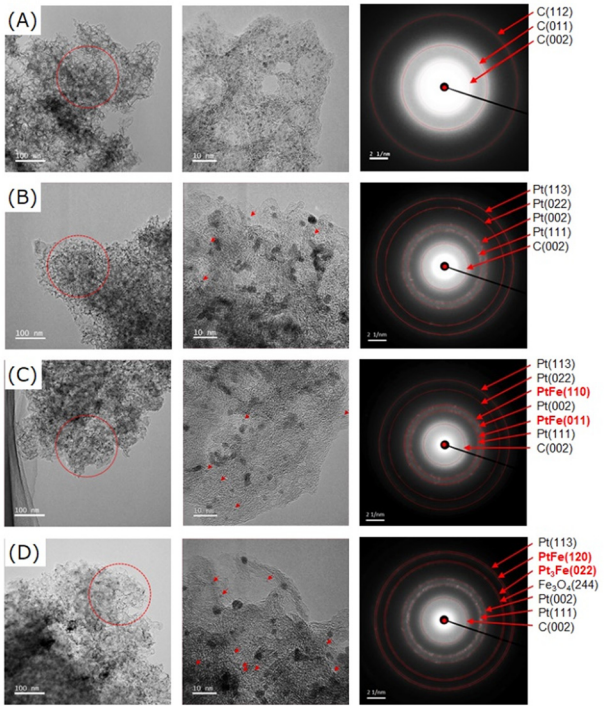

Fig. 7 TEM images and ED patterns for $(PtCl_n)_{0.9nm}$/Fe–N–C powder after (A) N = 0, (B) N = 25, (C) N = 50, and (D) N = 75. Red circles in the low-magnification TEM images (left row) indicate regions where ED patterns were obtained. Arrows in the high-magnification TEM images (middle row) indicate where $Pt_{subnano}$ is present.

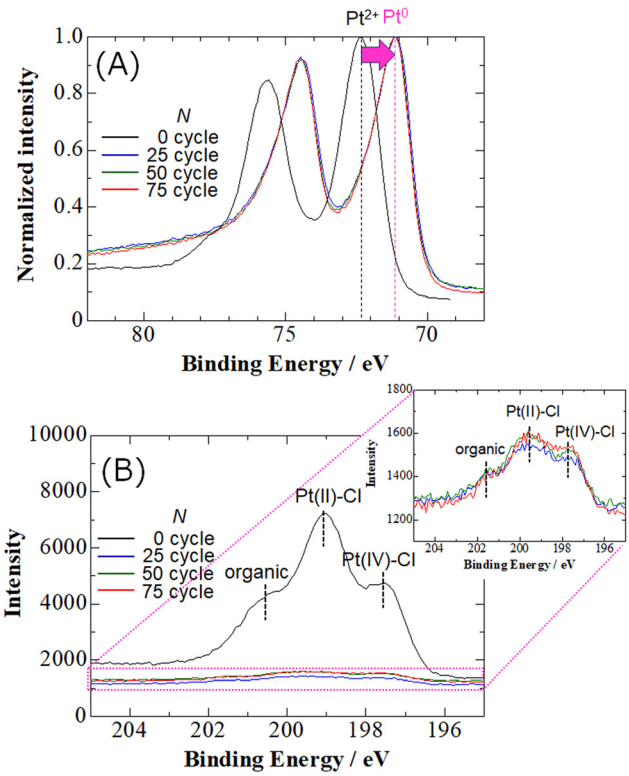

Fig. 8 XPS (A) Pt 4f and (B) Cl 2p spectra obtained from $(PtCl_n)_{0.9nm}$/Fe–N–C powders before and after potential cycles (N).

electrode is higher than that of the commercial Pt/C catalyst from the beginning of the *N*. As is well known that Pt alloy with Fe (and other nonprecious metals such as Co and Ni) has been recognized to be very effective in increasing of SA for the ORR.[6,29–33] This is because a Pt skin layer is formed on the surface of the Pt alloy nanoparticles[34–36] and its electronic state is modified by the alloy, which increases the apparent rate constant for the ORR[37,38] and the amount of oxygen adsorption.[39] This is of significant interest because it is not usually considered that Pt dissolves and alloying at such an early stage during AST of Pt nanoparticle catalysts. One possibility is that the chlorine atoms in $PtCl_n$ promote the dissolution of Pt. In the chlorine-free Pt/Fe–N–C catalyst ($PtCl_n$/Fe–N–C–HT(H_2) in Fig. 4), it is suggested that aggregation rather than dissolution of Pt dominates in the early stages of cycling.

The chemical state of Pt during the electrochemical reaction was investigated using *in situ* XAFS. Fig. 9 shows CVs, the change in the ECSA, and particle size distribution histograms as a function of *N*. Representative TEM images of the particle size distribution measurements, including the *N* = 0 results after *in situ* XAFS measurements, are shown in Fig. S7 in the SI. The average particle size was d = 0.9 ± 0.1 nm at *N* = 0 (pristine), as shown in Fig. 5(C). This value increased to 1.2 ± 0.3 nm after potential application (Fig. S7(A)) and further increased to 1.6 ± 0.4 nm after *N* = 25. Thus, the decrease in ECSA is due to an increase in particle size caused by Ostwald ripening.[40] Additionally, some agglomeration is beginning to occur, which could have a slight impact. On the other hand, the particle size distribution after *N* = 75 shows a clear shift toward smaller particles compared to the distribution for *N* = 25, with an average particle size of d = 1.5 ± 0.6 nm. The percentage of particles smaller than 1 nm increased from 8.6% (*N* = 25) to 15.6% (*N* = 75). ECSA value has also begun to increase. These results are specific phenomenon for $PtCl_n$/Fe–N–C and may be attributed to *in situ* $Pt_{subnano}$ formation. This is also consistent with the results of the TEM observations (shown in Fig. 7). Fig. 10 shows the change in the white

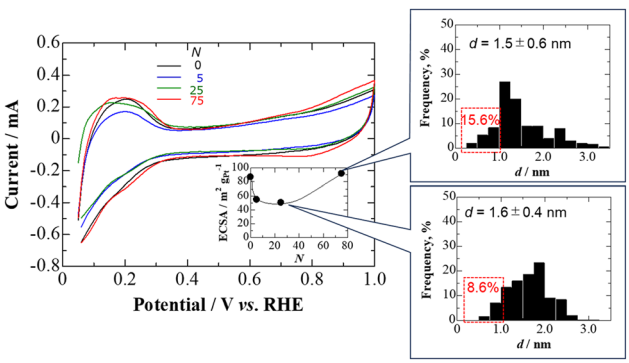

Fig. 9 Cyclic voltammograms employed to determine the ECSA values and particle size distribution histograms for Nafion-coated $(PtCl_n)_{0.9nm}$/Fe–N–C electrode in 0.1 M $HClO_4$ solution deaerated with N_2 at room temperature at a scan rate of 50 mV s^{-1}.

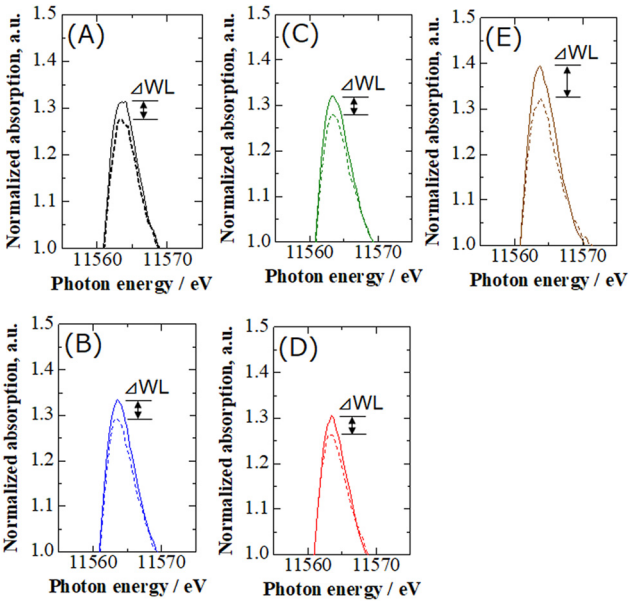

Fig. 10 XANES spectra of $(PtCl_n)_{0.9nm}$/Fe–N–C electrode with (A) *N* = 0, (B) *N* = 5, (C) *N* = 25, and (D) *N* = 75 and (E) commercial Pt/C (*N* = 0) at (----) 0.4 V and (—) 1.0 V in N_2-purged 0.1 M $HClO_4$.

line (WL) peak for the Pt-L3 edge X-ray absorption near edge fine structure (XANES) at 1.0 V and 0.4 V for the $(PtCl_n)_{0.9nm}$/Fe–N–C electrode after *N* = 0, 5, 25 and 75 cycles. Results for commercial Pt/C at *N* = 0 are also included for comparison. Full-scale XANES spectra are shown in Fig. S8 of the SI. The shape of the XANES spectra of $(PtCl_n)_{0.9nm}$/Fe–N–C at each cycle did not change significantly with the number of cycles at either 0.4 V or 1.0 V. This means that the Pt–Cl bond decreases immediately after the application of potential, regardless of *N* and indicates that the electronic state of the catalyst does not change with cycling. The WL intensity for all the samples was higher at 1.0 V than at 0.4 V, which confirms the oxidation (adsorption of oxygen species) of Pt at 1.0 V. However, the change of the WL intensity (ΔWL) for all of the $(PtCl_n)_{0.9nm}$/Fe–N–C samples (ΔWL = 0.04) was lower than that for commercial Pt/C (ΔWL = 0.07), which suggests that $PtCl_n$/Fe–N–C suppresses oxidation of the Pt surface in the high-potential region and that the catalytic performance is not easily degraded.

Examples of the Fourier transform (FT) fitting results for extended X-ray absorption fine structure (EXAFS) spectra are shown in Fig. S9 in the SI. The EXAFS of the Pt-L3 edge for all samples, obtained from FT, is shown in Fig. S10. The EXAFS spectra corresponding to the bulk samples,[23] *e.g.*, Pt-foil and $PtCl_2$, were fitted. Effective scattering amplitudes for Pt–Pt and Pt–Cl were calculated using FEFF and fitted by Artemis with the k range of 3–10 $Å^{-1}$ and R range of 1.7–3.4 Å. The coordination number (CN), bond length (R), and Debye Waller factor (σ) were fitted as variable parameters. The results for CN, R, and σ for the Pt–Pt and Pt–Cl bond obtained from curve fitting analysis are also summarized in Table S1 and S2. For the EXAFS fitting of the Pt–Cl bond, σ

was fixed, since the noise observed in the EXAFS oscillations is due to the inhomogeneous distribution of the catalyst on the electrode surface. However, this affected the fitting accuracy of the Pt–Cl bond, and the discussion based on the fitting results was difficult. The concentration of N atoms on the catalyst powder loading on the electrode substrate was very low and no Pt–N bonds (Radial distance = 1.8 Å)[23] could be identified (below detection limits). Fe-K edge XAFS spectra in the appropriate intensity range could not be obtained for the same reason. Therefore, the following discussion will focus on the Pt–Pt bond. Fig. 11 shows the changes in CN and *R* with respect to *N*. The CN values were almost the same for both 0.4 V and 1.0 V during the potential cycles, regardless of *N*. However, the *R* values at 1.0 V were longer than those at 0.4 V for all cycles, which suggests that the Pt–Pt bond length is increased by the surface adsorption of oxygen species. The changes in the CN and *R* values at each *N* are described in detail. At *N* = 0, the CN values for $PtCl_n$/Fe–N–C were lower or almost equal to those of commercial Pt/C, which is mainly due to the smaller particle size (*d* = 1.0 nm) than that for commercial Pt/C (*d* = 2.5 nm), and may also be slightly due to the reduction of Pt–Pt binding sites as a result of Cl binding to Pt. In contrast, the *R* values were higher than those of commercial Pt/C. The metal-to-metal bond length typically decreases with decreasing particle size;[41] however, there are exceptions. For example, when hydrogen is chemisorbed onto a Pt surface, the electron density between atoms decreases due to the electron-withdrawing properties of hydrogen, which results in longer interatomic distances.[41–43] In the case of $PtCl_n$, the chlorine adsorbed on the Pt surface also affects the electron density in the Pt atoms, which results in a higher *R* value than that for commercial Pt/C. This means that Pt particles dissolve easily. Furthermore, this is consistent with the results shown in Fig. 4, where Pt/Fe–N–C (without Cl_n) mainly causes Pt particle agglomeration in the initial stage of AST, while $PtCl_n$/Fe–N–C mainly causes dissolution and reprecipitation. In addition, it was newly inferred that the specific adsorption of Cl to Pt is one of the reasons why the initial SA_k value of $(PtCl_n)_{0.9nm}$/Fe–N–C is lower than that of $(PtCl_n)_{1.3nm}$/Fe–N–C (see Fig. 6). The CN values increased up to *N* = 25 cycles, which suggests that the desorption of Cl adsorbed on the Pt surface and the coarsening of the particles occurs within 20–30 cycles. In contrast, the *R* value decreases, which may be due to the desorption of Cl from Pt and the alloying of Pt and Fe. Kaito *et al.* reported that the Pt–Pt bond length for Pt shell–Au core alloy catalysts is shorter than that for Pt foil and Pt/C catalysts, which is the reason for their high ORR activity.[44,45] Even for the $PtCl_n$/Fe–N–C in the present study, the ED pattern for the alloy is clearly observed after only *N* = 50 cycles (see Fig. 7(C)). The ED pattern after 25 cycles (Fig. 7(B)) showed no alloy formation, although this may have been below the detection limit. The increase in the SA_k for the ORR (Fig. 6) is also consistent with the results reported by Kaito *et al.* The CN values also decreased again after *N* = 25 cycles, whereas the *R* value remained almost constant or increased only slightly. The symmetrical change in the CN and *R* values became asymmetrical after *N* = 25 cycles. The CN values increase as the Pt particles coarsen; therefore, the decrease in the CN values may reflect particle refinement (*i.e.*, the formation of $Pt_{subnano}$). In addition, the newly produced $Pt_{subnano}$ is not affected by chlorine, so that the increase in the *R* value is suppressed. These results indicate that coarsening and refinement occur repeatedly within a very short *N* period, which suggests an unprecedented mechanism.

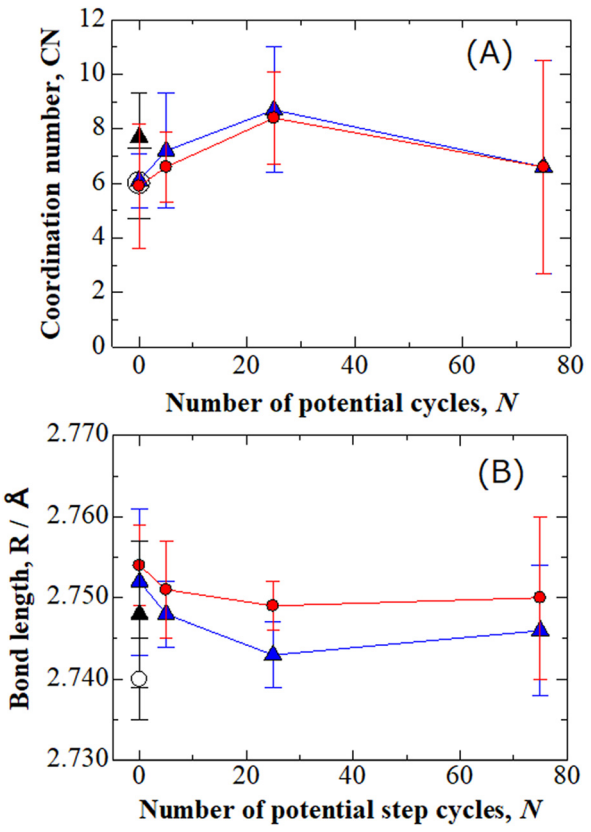

Fig. 11 (A) CN and (B) R as a function of *N*. The working electrode potentials were (▲) 0.4 V and (●) 1.0 V. The (▲) and (○) plots are the results for a commercial Pt/C electrode at 0.4 V and 1.0 V, respectively.

Conclusions

The $PtCl_n$/Fe–N–C catalyst exhibited superior activity and durability. Previous studies have shown that this is due to the trapping of dissolved Pt ions by Fe–N–C and the formation of new subnano-sized platinum particles. In this study, Pt chloride supported on Fe–N–C was found to be more soluble in solution as Pt ions than as pure Pt, and the formation of subnanoparticles occurs earlier in the potential cycle. The results also suggest that Pt aggregation and refinement occur repeatedly and dynamically during short periods of the

potential cycle (a few to several tens of cycles). The refinement rate is relatively dominant over the aggregation rate, therefore, the number of subnanoparticles continues to increase over a long period of time (thousands to tens of thousands of cycles). This is a newly elucidated mechanism for the high durability of the $PtCl_n$/Fe–N–C catalyst. In the long history of fuel cell catalyst development, no catalyst has ever achieved apparent high durability by this mechanism. We consider that new catalysts that consist of a combination of Fe–N–C and Pt have significant potential to be developed as next-generation high-performance catalysts. Furthermore, based on sufficient error analysis, we plan to conduct operando XAFS using a single cell to observe the dynamic process of repetitive aggregation and nanosizing. The results will be reported in a another MS.

Conflicts of interest

The author declares no conflicts of interest.

Data availability

Supplementary information: CV; hydrodynamic ORR voltammograms; I^{-1} *vs.* $\omega^{1/2}$ plots; image of electrochemical cell for *in situ* XAFS; XPS spectra; change in ECSA at single cell; TEM images and particle size distribution histograms of commercial Pt/C (pristine) and $(PtCl)_n$/Fe–N–C after *in situ* XAFS; XANES spectra; fitting results of EXAFS. See DOI: **https://doi.org/10.1039/D5LF00185D**.

The data will be made available to a public repository and are also available upon request to the corresponding author.

Acknowledgements

The author thanks Dr. Q. Yuan, Dr. M. Matsumoto (present affiliation: FC-Cubic TRA), and Dr. M. Arao (present affiliation: FC-Cubic TRA), all of the Nissan Arc Company, for their contributions to the *in situ* XAFS, XPS, and TEM measurements, and Dr. T. Saito (Toyota Boshoku Co.) for MEA evaluation, and also thanks FORTE Science Communications (**https://www.forte-science.co.jp/**) for English language editing.

References

1 **https://www.nedo.go.jp/content/800016621.pdf**.
2 B. C. Beard and P. N. Ross, *J. Electrochem. Soc.*, 1990, **137**, 3368–3373.
3 D. Wang, H. L. Xin, R. Hovden, H. Wang, Y. Yu, D. A. Muller, F. J. DiSalvo and H. D. Abruña, *Nat. Mater.*, 2013, **12**, 81–87.
4 Y.-H. Chung, D. Y. Chung, N. Jung, H. Y. Park, S. J. Yoo, J. H. Jang and Y.-E. Sung, *J. Phys. Chem. C*, 2014, **118**, 9939–9945.
5 M. Watanabe, K. Tsurumi, T. Mizukami, T. Nakamura and P. Stonehard, *J. Electrochem. Soc.*, 1994, **141**, 2659–2668.
6 H. Yano, M. Kataoka, H. Yamashita, H. Uchida and M. Watanabe, *Langmuir*, 2007, **23**, 6438–6445.
7 H. Kwon, M. K. Kabiraz, J. Park, A. Oh, H. Baik, S. Choi and K. Lee, *Nano Lett.*, 2018, **18**, 2930–2936.
8 H. Y. Kim, T. Kwon, Y. Ha, M. Jun, H. Baik, H. Y. Jeong, H. Kim, K. Lee and S. H. Joo, *Nano Lett.*, 2020, **20**, 7413–7421.
9 K. Okaya, H. Yano, K. Kakinuma, M. Watanabe and H. Uchida, *ACS Appl. Mater. Interfaces*, 2012, **4**, 6982–6991.
10 G. Jiang, H. Zhu, X. Zhang, B. Shen, L. Wu, S. Zhang, G. Lu, Z. Wu and S. Sun, *ACS Nano*, 2015, **9**, 11014–11022.
11 H. Tsunoyama, A. Ohnuma, K. Takahashi, A. Velloth, M. Ehara, N. Ichikuni, M. Tabuchi and A. Nakajima, *Chem. Commun.*, 2019, **55**, 12603–12606.
12 S. Zhu, X. Wang, E. Luo, L. Yang, Y. Chu, L. Gao, Z. Jin, C. Liu and W. Xing, *ACS Energy Lett.*, 2020, **5**, 3021–3028.
13 X. Wang, L. Zhao, X. Li, Y. Wang, Q. Yao, J. Xie, Q. Xue, Z. Yan, X. Yuan and W. Xing, *Nat. Commun.*, 2022, **13**, 1596–1605.
14 Y. Okamoto, *Chem. Phys. Lett.*, 2006, **429**, 209–213.
15 S. Gudmundsdóttir, E. Skúlason, K.-J. Weststrate, L. Juurlink and H. Jónsson, *Phys. Chem. Chem. Phys.*, 2013, **15**, 6323–6332.
16 H. Yano and K. Iwasaki, *Surfaces*, 2024, **7**, 472–481.
17 F. A. Viva, M. M. Bruno, E. A. Franceschini, Y. R. J. Thomas, G. R. Sanchez, O. S. Feria and H. R. Corti, *J. Hydrogen Energy*, 2014, **39**, 8821–8826.
18 Z. Yang, J. Ren, Z. Zhang, X. Chen, G. Guan, L. Qiu, Y. Zhang and H. Peng, *Chem. Rev.*, 2015, **115**, 5159–5223.
19 V. Yarlagadda, N. Ramaswamy, R. S. Kukreja and S. Kumaraguru, *J. Power Sources*, 2022, **532**, 231349.
20 Y. Luo, K. Li, Y. Chen, J. Feng, L. Wang, Y. Jiang, L. Li, G. Yu and J. Feng, *Adv. Mater.*, 2023, **35**, 2300624.
21 Y. Sha, J. Ji, S. Li, X. Gao, B. Zhang, M. Ling, C. Liang and Z. Lin, *Eur. J. Inorg. Chem.*, 2020, 165–168.
22 F. Xiao, Q. Wang, G.-L. Xu, X. Qin, I. Hwang, C.-J. Sun, M. Liu, W. Hua, H. Wu, S. Zhu, J.-C. Li, J.-G. Wang, Y. Zhu, D. Wu, Z. Wei, M. Gu, K. Amine and M. Shao, *Nat. Catal.*, 2022, **5**, 503–512.
23 H. Yano and K. Iwasaki, *ACS Omega*, 2024, **9**, 27499–27508.
24 H. Kishi, T. Sakamoto, K. Asazawa, S. Yamaguchi, T. Kato, B. Zulevi, A. Serov, K. Artyushkova, P. Atanassov, D. Matsumura, K. Tamura, Y. Nishihata and H. Tanaka, *Nanomaterials*, 2018, **8**, 965–978.
25 M. Primbs, Y. Sun, A. Roy, D. Malko, A. Mehmood, M.-T. Sougrati, P.-Y. Blanchard, G. Granozzi, T. Kosmala, G. Daniel, P. Atanassov, J. Sharman, C. Durante, A. Kucernak, D. Jones, F. Jaouen and P. Strasser, *Energy Environ. Sci.*, 2020, **13**, 2480–2500.
26 M. Watanabe and S. Motoo, *J. Electroanal. Chem. Interfacial Electrochem.*, 1975, **60**, 275–283.
27 H. Uchida, N. Ikeda and M. Watanabe, *J. Electroanal. Chem.*, 1997, **424**, 5–12.
28 **http://fccj.jp/pdf/19_01_kt.pdf**.
29 S. Mukerjee, S. Srinivasan, M. P. Soriaga and J. McBreen, *J. Electrochem. Soc.*, 1995, **142**, 1409–1422.
30 T. Toda, H. Igarashi, H. Uchida and M. Watanabe, *J. Electrochem. Soc.*, 1999, **146**, 3750–3756.

31 T. Toda, H. Igarashi and M. Watanabe, *J. Electroanal. Chem.*, 1999, **460**, 258–262.
32 T. Toda and I. Honma, *Trans. Mater. Res. Soc. Jpn.*, 2003, **28**, 215–220.
33 M. Chiwata, H. Yano, S. Ogawa, M. Watanabe, A. Iiyama and H. Uchida, *Electrochemistry*, 2016, **84**, 133–137.
34 L.-J. Wan, T. Moriyama, M. Ito, H. Uchida and M. Watanabe, *Chem. Commun.*, 2002, 58–59.
35 H. Uchida, H. Ozuka and M. Watanabe, *Electrochim. Acta*, 2002, **47**, 3629–3636.
36 S. Kobayashi, M. Aoki, M. Wakisaka, T. Kawamoto, R. Shirasaka, K. Suda, D. A. Tryk, J. Inukai, T. Kondo and H. Uchida, *ACS Omega*, 2018, **3**, 154–158.
37 N. Wakabayashi, M. Takeichi, H. Uchida and M. Watanabe, *J. Phys. Chem. B*, 2005, **109**, 5836–5841.
38 H. Yano, J. M. Song, H. Uchida and M. Watanabe, *J. Phys. Chem. C*, 2008, **112**, 8372–8380.
39 M. Wakisaka, H. Suzuki, S. Mitsui, H. Uchida and M. Watanabe, *J. Phys. Chem. C*, 2008, **112**, 2750–2755.
40 O. F. Devereux, *Topics in Metallurgical Thermodynamics*, John Wiley, New York, 1983.
41 B. Delley, D. E. Ellis, A. J. Freeman, E. J. Baerends and D. Post, *Phys. Rev. B: Condens. Matter Mater. Phys.*, 1983, **27**, 2132–2144.
42 E. S. Marcos, A. P. J. Jansen and R. A. Van Santen, *Chem. Phys. Lett.*, 1990, **167**, 399–406.
43 M. K. Oudenhuijzen, J. H. Bitter and D. C. Koningsberger, *J. Phys. Chem. B*, 2001, **105**, 4616–4622.
44 T. Kaito, H. Mitsumoto, S. Sugawara, K. Shinohara, H. Uehara, H. Ariga, S. Takakusagi, Y. Hatakeyama, K. Nishikawa and K. Asakura, *J. Phys. Chem. C*, 2014, **118**, 8481–8490.
45 T. Kaito, H. Tanaka, H. Mitsumoto, S. Sugawara, K. Shinohara, H. Ariga, H. Uehara, S. Takakusagi and K. Asakura, *J. Phys. Chem. C*, 2016, **120**, 11519–11527.